communications physics

ARTICLE

https://doi.org/10.1038/s42005-023-01458-9 OPEN

Sign reversal diode effect in superconducting Dayem nanobridges

Daniel Margineda[1,4✉], Alessandro Crippa[1], Elia Strambini[1], Yuri Fukaya[2], Maria Teresa Mercaldo[3], Mario Cuoco[2] & Francesco Giazotto[1✉]

Supercurrent diodes are nonreciprocal electronic elements whose switching current depends on their flow direction. Recently, a variety of composite systems combining different materials and engineered asymmetric superconducting devices have been proposed. Yet, ease of fabrication and tunable sign of supercurrent rectification joined to large efficiency have not been assessed in a single platform so far. We demonstrate that all-metallic superconducting Dayem nanobridges naturally exhibit nonreciprocal supercurrents under an external magnetic field, with a rectification efficiency up to ~ 27%. Our niobium nanostructures are tailored so that the diode polarity can be tuned by varying the amplitude of an out-of-plane magnetic field or the temperature in a regime without magnetic screening. We show that sign reversal of the diode effect may arise from the high-harmonic content of the current phase relation in combination with vortex phase windings present in the bridge or an anomalous phase shift compatible with anisotropic spin-orbit interactions.

[1] NEST Istituto Nanoscienze-CNR and Scuola Normale Superiore, I-56127 Pisa, Italy. [2] SPIN-CNR, I-84084 Fisciano, (SA), Italy. [3] Dipartimento di Fisica "E. R. Caianiello", Università di Salerno, I-84084 Fisciano, (SA), Italy. [4] Present address: CIC nanoGUNE BRTA, E-20018 Donostia-San, Sebastián, Spain. ✉email: d.margineda@nanogune.eu; francesco.giazotto@sns.it

Non-reciprocal charge transport is an essential element in modern electronics as a building block for multiple components such as rectifiers, photodetectors, and logic circuits. For instance, pn-junctions and Schottky-barrier devices are archetypal semiconductor-based examples of systems, known as *diodes*, with direction-selective charge propagation. Their operation stems from the spatial asymmetry of the heterojunction that provides inversion symmetry breaking. Likewise, dissipationless rectification refers to the asymmetric switching of the critical current (I_{sw}) required to turn a superconductor into the normal state depending on the current bias polarity. Breaking both inversion and time-reversal symmetry, which are preserved in conventional superconductors, is the foundational aspect to enable the diode effect, as recently observed in superconducting materials[1–4] and heterostructures[5–12]. Recent experimental findings have boosted a number of theoretical investigations in superconductors[13–16] and Josephson junctions (JJs)[17–19]. In particular, several mechanisms have been proposed to account for the supercurrent diode effect (SDE). On the one hand, those based on intrinsic depairing currents focus on finite momentum pairing that arise from the combination of spin-orbit coupling (SOC) and Zeeman field[13–16,20], or from Meissner currents[18]. On the other hand, other works underline the role of Abrikosov vortices, magnetic fluxes, screening currents or self-field effects as key elements for setting out nonreciprocal charge transport in superconductors[21–26], such as in systems with trapped Abrikosov vortices[27–29] or in micron-sized Nb-based strips[30–34].

Till now, most of the research efforts have aimed to the realization of a SDE that maximizes the rectification efficiency, while the change of its polarity has been reported in a few cases only[6,10,11,35–37]. The SDE sign reversal has been interpreted as a consequence of finite momentum pairing[6,11,35,36] requiring in-plane magnetic fields or diamagnetic currents and Josephson vortices[10,29], as well as ascribed to vortex ratchet and asymmetric pinning effects[38–41]. All these outcomes suggest the need for an effective mastering of the polarity change of the SDE and its implementation in a simple and monolithic platform suitable for nanoscale miniaturization, not accomplished yet.

Here, we experimentally demonstrate a sign reversal tunable SDE in elemental superconducting weak links made on niobium (Nb). Nano-sized constrictions of Nb realize Dayem bridges whose switching currents for positive and negative sweep direction, I_{sw}^{+} and I_{sw}^{-}, respectively, differ in the absolute value. This difference can be tuned both in amplitude and sign by an out-of-plane magnetic field (B_z), without inverting the polarity of B_z. Thermal effects can lead to two different energy scales for the maximal amplitude and the sign reversal of the diode efficiency which is inconsistent with physical scenarios related to Meissner currents or self-field effects. We show that sign reversal of the non-reciprocal response may arise from the phase shift due to the vortex phase winding or from spin-orbit effects due to the material granularity, in either case jointly with a few-harmonic content of the current-phase relation (CPR) of the weak link.

Results

Metallic diode architectures. We analyze two different geometries of Nb Dayem bridges, i.e., weak links made of a constant-thickness and all-metallic constriction between two superconducting banks[42]. The schematics of the electronic circuitry and false-color scanning electron micrographs of the devices are shown in Fig. 1a. In the first type of samples, 25-nm-thick micrometer-wide banks are connected via a link whose length l is ~ 80 nm and width w ~ 180 nm. The second type consists of 55-nm-thick banks connected via a quasi-one-dimensional wire with $l \simeq 1$ μm, and $w \simeq 80$ nm. Hereafter, we shall refer to the first and second types of bridges as short and long, respectively. Both device families are patterned through a single electron-beam lithography step followed by sputter deposition of the Nb thin film and lift-off. A 4-nm-thick Ti layer is pre-sputtered for adhesion purposes.

The differential resistance $R = dV/dI$ versus temperature T of two representative bridges is shown in Fig. 1b. The first abrupt reduction of R marks the critical temperature of the Nb films $T_{TF} \simeq 8.1(7.9)$ K for the 55(25)-nm-thick sample, suggesting minor impact of the film thickness on the superconducting state. The resistance drops to zero at the critical temperature of the weak link (T_c), which strongly depends, along with its normal-state resistance R_N, on the geometry[42]. While the short bridge exhibits $R_N \sim 40\ \Omega$, in the long one has $R_N \sim 270\ \Omega$.

Below T_c, dissipationless transport occurs in the bridges owing to Cooper pairs supercurrent. The temperature dependence of the switching current I_{sw} of both devices is displayed in Fig. 1c. From the fit to the Bardeen equation $I_{sw}(T) = I_{sw}^{0}[1 - (\frac{T}{T_c})^2]^{\frac{3}{2}}$, we extract a zero-temperature switching current $I_{sw}^{0} \simeq 720\,\mu$A and a critical temperature $T_c^S \simeq 4.3$ K for the shor bridge. Similarly, for the long weak link we obtain $I_{sw}^{0} \simeq 42\,\mu$A and $T_c^L \simeq 2.1$ K. From these values, we determine a zero-temperature BCS energy gap $\Delta_0 = 1.764 k_B T_c^{S(L)} \simeq 650(320)\,\mu$ eV for the short(long) bridge, where k_B is the Boltzmann constant. For the long bridge, we deduce a superconducting coherence length $\xi_0 = \sqrt{\hbar l/(R_N w t e^2 N_F \Delta_0)} \simeq 11$ nm, where t is the film thickness, $N_F \simeq 5.33 \times 10^{47} J^{-1} m^{-3}$ is the density of states at the Fermi level of Nb[43], and e is the electron charge. Similarly, we can evaluate the London penetration depth $\lambda_L = \sqrt{\hbar R_N w t/(\pi l \mu_0 \Delta_0)} \simeq 790$ nm, where μ_0 is the vacuum magnetic permeability. Since $w, t \ll \lambda_L$, the bridges can be uniformly penetrated by an external magnetic field.

The current vs voltage (IV) characteristics of the short and long bridges are shown in Fig. 1d, e, respectively, for selected values of bath temperature. The devices show an abrupt transition to the normal state at the switching current I_{sw} and display the typical hysteresis of metallic junctions which originates from Joule heating induced in the bridge when the bias current is swept back from the resistive to the dissipationless state[44].

Short Dayem bridge diode performance. Let us now discuss how the short Dayem bridge in Fig. 1a can be used as a supercurrent diode. Non-reciprocal dissipationless transport is revealed by comparing the switching currents while sweeping the biasing current from zero to positive values (I_{sw}^{+}) or from zero to negative values (I_{sw}^{-}) in the presence of an out-of-plane magnetic field B_z. The switching currents at $T = 0.3$ K are reported in Fig. 2a. The magnetic field increasingly reduces the superconducting gap and thereby both the switching currents. A linear decrease in B_z of I_{sw}^{+} and $|I_{sw}^{-}|$ is observed up to ~0.07 T. At larger fields, the dependence of the switching currents on B_z is sublinear. Notably, both $I_{sw}(B_z)$ are not antisymmetric with respect to the magnetic field ($I_{sw}(B_z) \neq I_{sw}(-B_z)$) while the symmetry relation $I_{sw}^{+}(B_z) \simeq -I_{sw}^{-}(-B_z)$ is respected, within the small experimental fluctuations, as theoretically expected. This symmetry relation is further confirmed in the switching currents difference $\Delta I_{sw} \equiv I_{sw}^{+} - |I_{sw}^{-}|$ displaying an odd-in-B_z superconducting diode effect ($\Delta I_{sw}(B_z) \simeq -\Delta I_{sw}(-B_z)$) as shown in Figure 2b. ΔI_{sw} is characterized by a maximum at $B_{max} \simeq 0.05$ T and a sign inversion at $B_R \simeq 0.1$ T where I_{sw}^{+} and $|I_{sw}^{-}|$ have a crossing (see Fig. 2a). From now on, B_{max} indicates the position in field of the rectification peak. Two IV curves, recorded for magnetic fields lower and larger than B_R, are plotted in Fig. 2c to emphasize the sign change in the rectification.

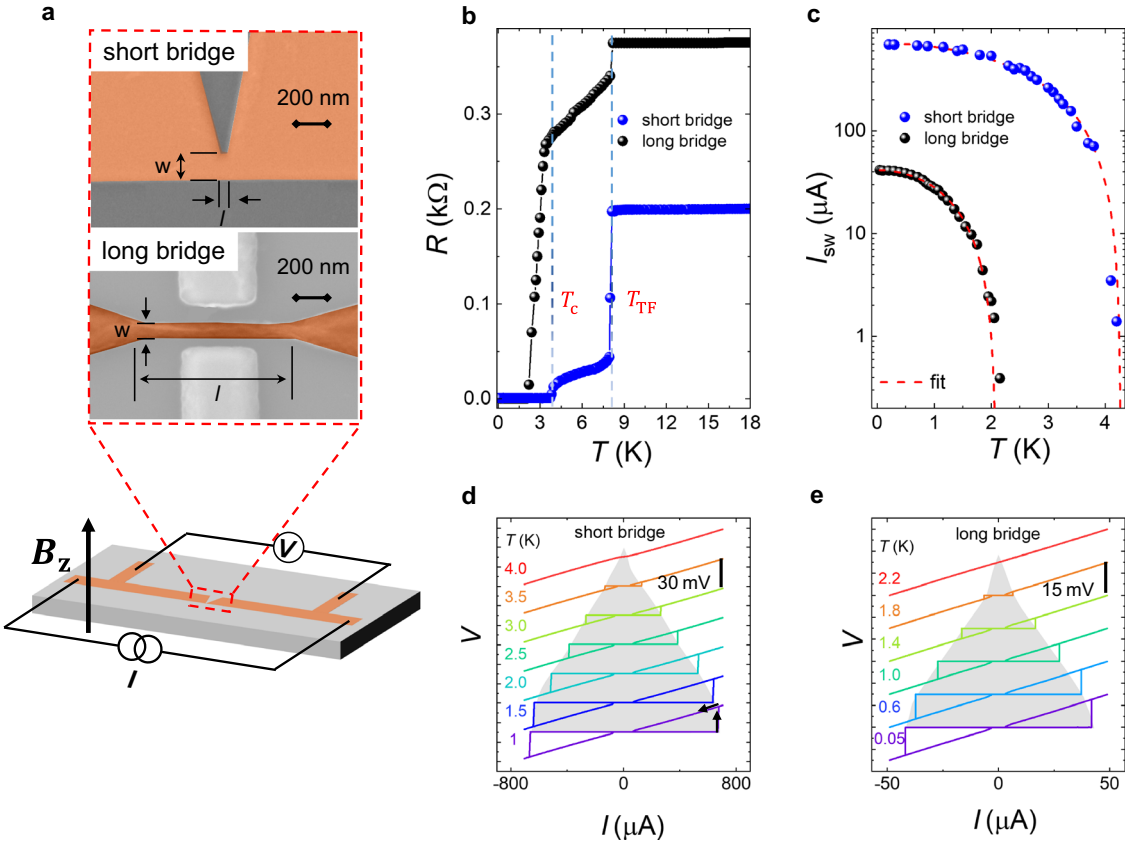

Fig. 1 Nb Dayem nanobridge diodes and basic electrical characterization. a Samples and schematic setup to measure the voltage characteristics V as a function of a bias current I with an applied out-of-plane magnetic field B_z. In the upper part, scanning electron micrographs of two weak links with different length l and width w: one is a constriction of Nb strip (with characteristic dimensions $l \sim 80$ nm and $w \sim 180$ nm), the other is a quasi-1D wire ($l \sim 1$ μm, $w \sim 80$ nm) connecting the banks; they are labeled as short and long, respectively. The electrodes used in the experiment are false-colored in orange. **b** Temperature dependence of the zero-bias resistance for the two Dayem bridges. Thin film (T_{TF}) and weak link (T_c) critical temperatures are marked by dashed lines for the short device. **c** Temperature (T) dependence of the switching supercurrents for the short (blue dots) and the long (black dots) bridges. Red dashed lines are the fit to Bardeen equation, as described in the text. IV characteristics of the short, **d**, and long bridge, **e**. The curves are vertically offset for clarity, and the superconducting region is highlighted in grey to visualize the temperature-induced decay of the dissipationless current. Black arrows indicate the direction of the bias current swept back and forth starting at zero amplitude.

Nonreciprocal transport can be conveniently quantified by the rectification efficiency defined as $\eta = \frac{I_{sw}^{+} - |I_{sw}^{-}|}{I_{sw}^{+} + |I_{sw}^{-}|}$. Figure 2d shows the evolution of η versus B_z and T. $\eta(B_z)$ is substantially unaffected by thermal effects up to $T \simeq 1.75$ K $= 0.41\ T_c^S$ where a maximum rectification $\eta_{\max} \sim 27\%$ is obtained. The evolution of η_{max} in temperature is displayed in Fig. 2e (i). In addition, we parametrize the diode sensitivity to the magnetic field in the vicinity of the abrupt sign change as $\Gamma = \eta_{\max}/(|B_{\max} - B_R|)$. A maximum value $\Gamma \sim 650\ \mathrm{T}^{-1}$ is achieved around 2.25 K (see Fig. 2e (i)) At higher temperatures, the quantities $\eta_{\max}$ Γ, and the characteristic magnetic fields $B_{\max}$ and B_R related to rectification (see Fig. 2e (ii)), all decrease in a similar fashion. The full profile of the rectification efficiency versus B_z is better visualized in Fig. 2f where $\eta(B_z)$ is plotted for a few selected values of temperature.

Long Dayem bridge diode performance. Next, we characterize the long nanobridge shown in Fig. 1a. Figure 3a reports the decay of I_{sw}^{+} and $|I_{sw}^{-}|$ as a function of B_z. At first, we notice that the switching currents are damped down to ~ 60% of their zero-field value at $B_z \simeq 0.3$ T, whereas in the previous sample, the same damping is achieved for lower fields ($B_z \simeq 0.07$ T see Fig. 2a). Figure 3b displays ΔI_{sw} versus B_z. For low magnetic fields, $\Delta I_{sw}(B_z)$ exhibits a linear relation. While increasing $|B_z|$ further, ΔI_{sw} bends and then inverts its trend: an abrupt jump realizes a sign reversal at $|B_R| \sim 0.34$ T. Then, a relative peak at $|B_{max}| \simeq 0.38$ T, marked by a red dashed line, represents the field at which maximum rectification efficiency is achieved as before. Next to the sign change, ΔI_{sw} leaves the clean trend and looks noisy. Such small jumps are reproducible, thus ruling out a stochastic nature of the underlying processes. Finally, ΔI_{sw} oscillates at higher magnetic fields, as shown in the inset of Fig. 3b. Two IV curves, for fields lower and larger than B_R, are plotted in Fig. 3c to highlight that the rectification sign changes from negative to positive as the field $B_z > 0$ increases contrary to the short bridge. This change in symmetry is attributed to the vortex nucleation as discussed later.

The magnetic field and temperature dependence of the rectification efficiency η is presented as a color plot in Fig. 3d. The sign change and the maximum rectification are affected by temperature in a different way as compared to the short constriction. The linear increase of the rectification at low fields smears out with temperature, reducing B_R until it vanishes at $T \simeq 1.1$ K $= 0.5\ T_c^L$. Rectification parameters displayed in Fig. 3e shows that B_{max} is more robust in temperature than B_R: it is still observable at $T \simeq 1.8$ K $= 0.8\ T_c^L$. The sudden change of sign is quantified by a maximum $\Gamma \sim 360\ \mathrm{T}^{-1}$ at 0.15 K. As before, the profile of rectification efficiency as a function of B_z is shown in

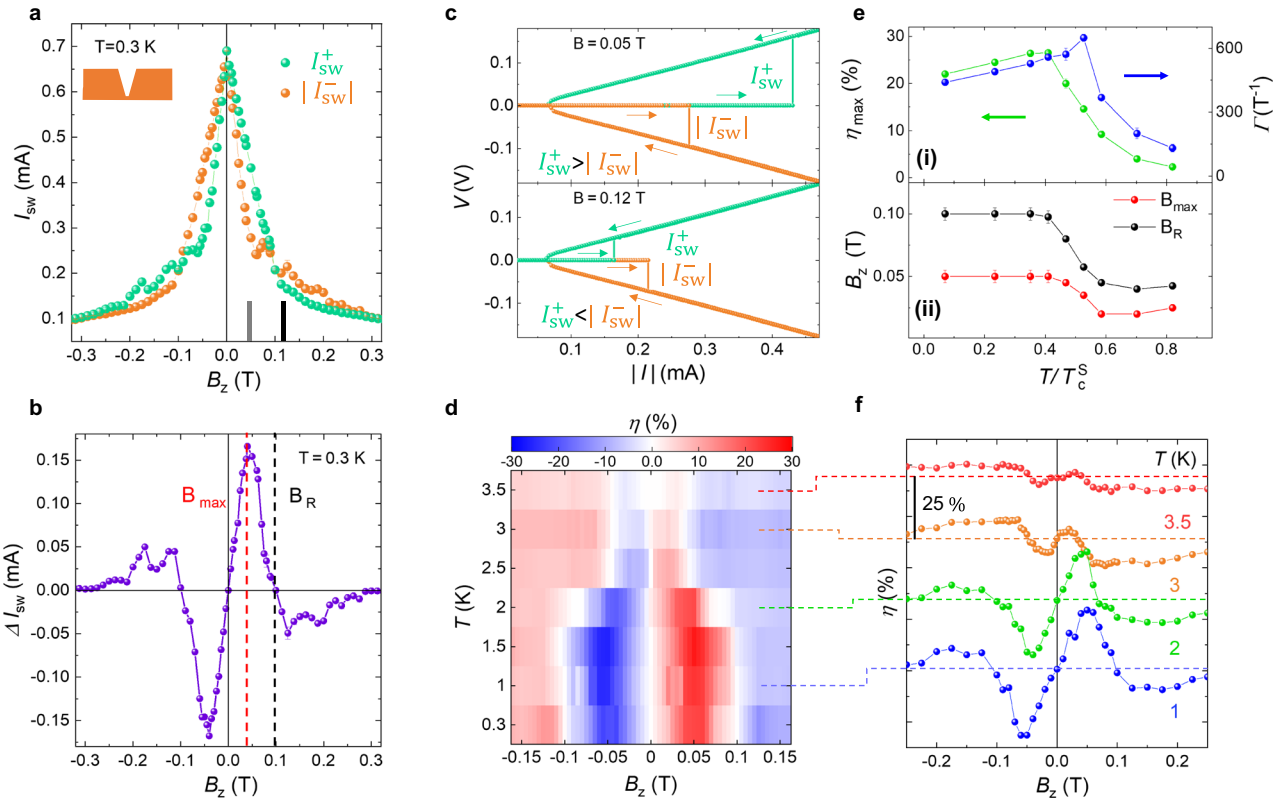

Fig. 2 Diode effect in a short Dayem bridge. a Out-of-plane magnetic field dependence of the switching current for positive I_{sw}^{+} (green dots) and negative $|I_{sw}^{-}|$ (orange dots) bias current recorded at 300 mK. **b**, ΔI_{sw} obtained from **a**. The magnetic field values at which the maximum (B_{max}) and sign reversal (B_R) of the rectification occur are marked by red and black dashed lines, respectively. **c,** *IV* curves with positive $I_{sw}^{+}>|I_{sw}^{-}|$ and negative $I_{sw}^{+}<|I_{sw}^{-}|$ rectification recorded at the magnetic fields marked by bars in panel **a**. **d** Color plot of the rectification efficiency $\eta(B_z, T)$ versus bath temperature and magnetic field. **e** Rectification parameters: $\eta_{max} \equiv (\eta_{max}(B_z > 0) + \eta_{max}(B_z < 0))/2$ (green dots), field-to-rectification efficiency transfer function Γ (blue dots) (**i**), B_{max} (red dots) and B_R (black dots) magnetic fields (ii) versus normalized temperature. T_c^S denotes the critical temperature of the short bridge. η_{max} is the rectification value of the low-field peak at B_{max}. **f** $\eta(B_z)$ for selected values of bath temperature marked by dashed lines in panel **d**. Curves are vertically offset for clarity. $\eta(B_z)$ function exhibits two extrema, below and above B_R. The rectification peak η_{max}, identified by B_{max}, decreases in magnitude and field for $T \geq 1.75$ K $= 0.4\ T_c^S$, until the minimum in the rectification at $B > B_R$ becomes an absolute extremum at T = 3 K (orange dots). For discussion, we keep B_{max} and η_{max} as the nomenclature for the maximum rectification.

Fig. 3f for a few selected values of temperature. The difference in the temperature trend between B_R and B_{max} (see Fig. 3e (ii)) suggests two different energy scales responsible for the sign reversal and the maximum rectification, as confirmed by measurements obtained in other devices with same nominal dimensions. (see Supplementary Figure 1). Rectification on the second sample exhibits similar $\eta(B_z)$ lineshape with almost identical B_{max} and η_{max} values and temperature dependence. In this sample, low-field features fade more rapidly with temperature, which appears to be sample-dependent.

Modeling the sign reversal of the diode effect. Previous SDE reported in conventional superconductor are normally attributed to Abrikosov vortices and self-field effects[29,34] or Meissner currents[30–33]. We have neglected those mechanisms since they are weak in amplitude. Such a conclusion can be directly deduced from the stark contrast of the profile of the switching current vs B-field data points. In both scenarios $I_{sw}(B_z)$ reaches a maximum at nonzero magnetic fields. Moreover, amplitude asymmetry does not change sign as a function of the magnetic field without reversing its orientation before the critical current vanishes. Instead, the switching current-field profile in our devices decays monotonically at low fields with no signature of the characteristic skewness. For this reason, we propose two physical scenarios compatible with our devices that may explain our experimental findings. Both of them rely on non-sinusoidal CPRs, typical of superconducting nanobridges[42], combined with an inversion-symmetry breaker. In model I, this is represented by a supercurrent vortex, while in model II by spin-orbit couplings. An out-of-plane magnetic field parametrized by B^* is considered, where B^* is given by the zero rectification field $\eta(B^*) = 0$ and by the vanishing of high-harmonic amplitude.

In model I, the Dayem nanobridge is schematized as a one-dimensional chain of weak links of width w formed by the Nb grains. A supercurrent vortex can nucleate in one of these weak links[45,46], as sketched in Fig. 4a, which induces a phase winding in the superconducting order parameter. These vortices have a typical size of the order of ξ, so only a few of them can be accommodated within the bridge. Notice that such vorticity is not a screening of the B-field, since the small dimensions of the bridge ($w \ll \lambda_L$) allow full penetration of B_z. In this framework, the CPR is affected by two-phase shifts: the conventional vector potential associated with B_z and the phase winding of the vortex. It is indeed the interplay of these two contributions that is responsible for a sign change in the rectification parameter. Though on a different length scale, this physical scenario is similar to that of Josephson phase vortices[29,47]. The rectification parameter η is then evaluated by determining the maximum and minimum values of the Josephson current with respect to the phase bias, see Methods for details.

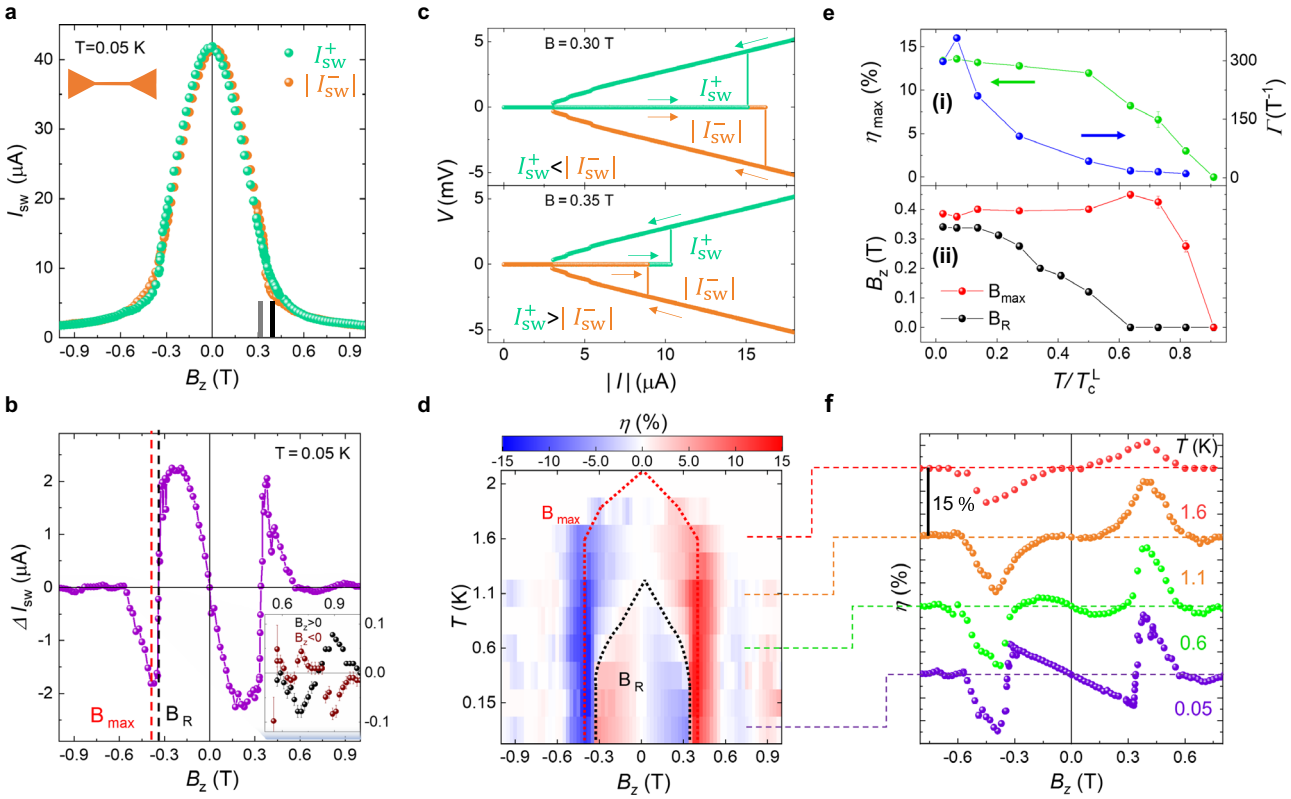

Fig. 3 Diode effect in a long Dayem bridge. a Magnetic field dependence of the switching current for positive I^+_{sw}(green dots) and negative $|I^-_{sw}|$(orange dots) bias current recorded at 50 mK. **b** ΔI_{sw} obtained from panel **a**. The rectification efficiency increases linearly in B_z until $|B_z| \simeq 015$ T. Red and black dashed lines mark the magnetic field values corresponding to sign reversal (B_R) and maximum rectification (B_{max}), respectively. Inset: Blow-up of ΔI_{sw} for large positive (black) and negative (brown) fields displaying several changes of signs. **c** *IV* characteristics with negative $I^+_{sw}<|I^-_{sw}|$ and positive $I^+_{sw}>|I^-_{sw}|$ rectification recorded at the magnetic fields marked by bars in panel **a**. **d** Color plot of the rectification efficiency as a function of temperature and magnetic field, $\eta(B_z, T)$. Dashed lines are guides for the eye to highlight the different temperature trends in B_{max} and B_R. **e** Rectification parameters: $\eta_{max} \equiv (\eta_{max}(B_z > 0) + \eta_{max}(B_z < 0))/2$ (green dots), field-to-rectification efficiency transfer function Γ (blue dots) (i), B_{max} (red dots) and B_R (black dots) magnetic fields (ii) versus normalized temperature. T^L_c denotes the critical temperature of the long bridge. η_{max} is the rectification value of the low-field peak at B_{max}. **f** η_{B_z} for selected bath temperatures marked by dashed lines in panel **d**. Curves are vertically offset for clarity.

Figure 4b, reports the evolution of η in B for different amplitudes of the second harmonic, I_2, of the CPR. The magnitude of η scales with I_2 showing multiple nodes, whose position in B is independent of I_2. The sign change also depends on the position of the vortex, as displayed in Fig. 4c, where $\eta(B)$ is evaluated for a vortex nucleated at different distances from the lateral edge of the bridge (x_v). This behavior suggests a phase-shift competition dominated at low fields by the vortex phase slip and at large fields by the vector potential.

Another scenario able to describe the sign reversal in the diode rectification can be envisioned by combining the colored CPR of the nanobridge with an anomalous phase shift[14,48–51] induced by spin-orbit interactions and magnetic fields. Nb is a heavy metal and thus possesses an atomistic spin-orbit interaction of the order of ~ 100 meV[52]. We extend such concept to our weak links where we call for a spin-orbit coupling of the order of a few meV, i.e., 2 orders of magnitude weaker than the atomic limit[53]. In particular, we can expect that mirror symmetry can be locally or globally broken in polycrystalline films[54], thereby leading to spin-orbit interaction of both Rashba and Dresselhaus types (see Methods). Figure 4d shows a sketch of the bridge modeled as an effective *SS′S* structure, where the *S* and *S′* components have different amplitudes of the superconducting gap and different spin-orbit couplings breaking horizontal and vertical mirror symmetries. The anisotropic spin-orbit interaction generates an anomalous phase shift in the CPR that varies with the magnetic field, as explicitly shown in Supplementary Figure 2. The anomalous phase is then introduced in the CPR via a phenomenological parameter Γ_B providing a first-order cosine component in the Fourier expansion, i.e., $I = \sum_n I_n \sin(\varphi) + \Gamma_B \cos(\varphi)$ (see Methods for details). The anomalous phase φ_0 is then related to the amplitude of Γ_B. We assume a linear damping of the harmonics $I_n = I_{n,0}(1 - B/B^*)$, which defines the scale parameter B^*.

From model II, the diode sign reversal takes place only in the presence of a sizable third harmonic component. Figure 4e reports $\eta(B)$ for some values of $I_{3,0}$. By increasing $I_{3,0}$, the sign inversion gets more pronounced, whereas the maxima and minima of the rectification ($B^s_{max} \simeq 0.74B^*$, $B^s_{\min} \simeq 0.89B^*$) are barely affected by the weight of the harmonic. Moreover, by including more harmonics in the CPR, the lineshape of $\eta(B)$ is modified. For instance, Figure 4f shows that a fourth-order harmonic affects the magnetic field dependence by substantially removing the sign change.

Discussion

The comparison between our experimental findings and the proposed models reveals some important features supporting the proposed mechanisms. In particular, for both bridges η has an almost monotonic damping in temperature that can be explained in both models by the reduction of high-order harmonics. This is expected in long metallic weak links where the CPR evolves from

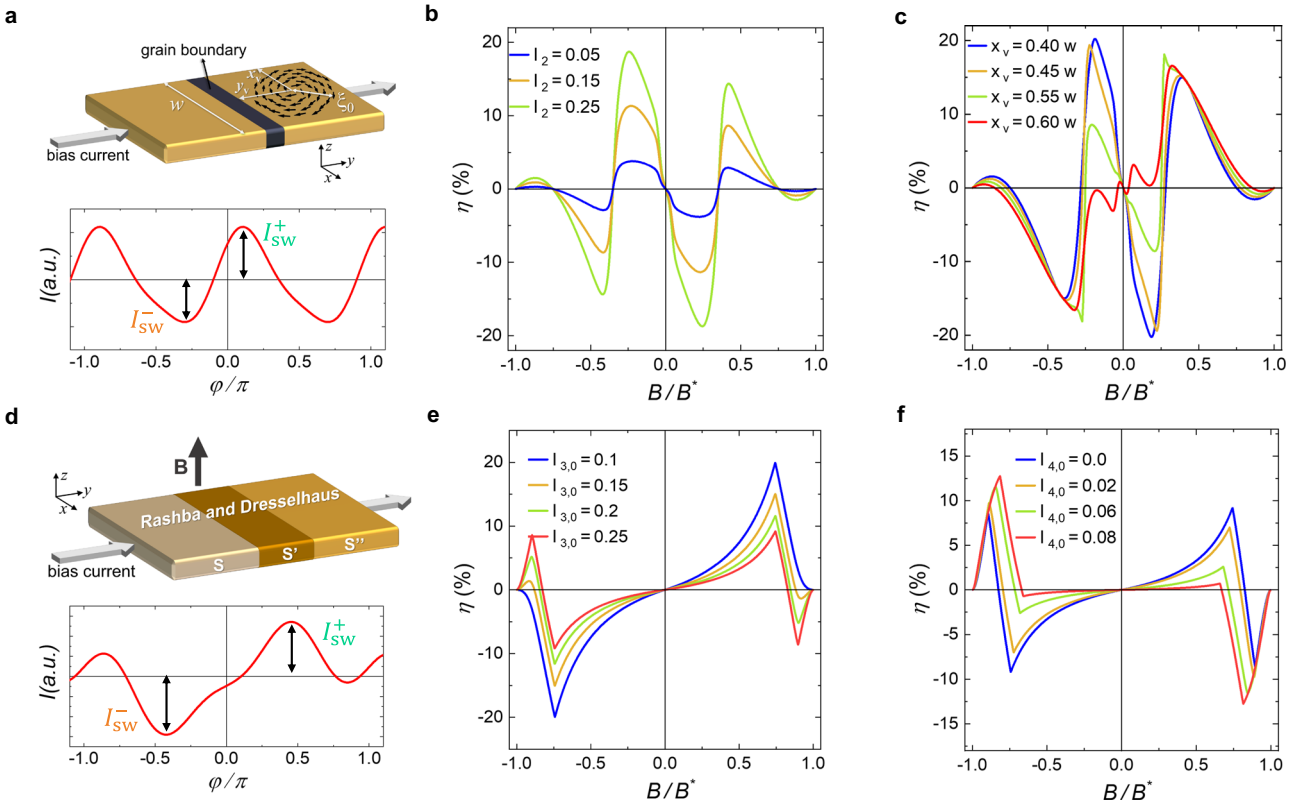

Fig. 4 Modelling supercurrent across a nanobridge for sign-tunable diode effect. a Sketch of the theoretical framework for model I, with the arrows indicating the phase winding associated with a vortex nucleated near the grain boundary. Characteristic CPR (red line) of the weak link hosting a vortex close to the grain boundary. **b** Nonreciprocal rectification efficiency η calculated for a few values of the second harmonic at a given position of the vortex core with $(x_v, y_v) = (0.4\,w, 0.4\,w)$ and $\gamma_v = 1$. **c** Nonreciprocal rectification efficiency η for different positions (x_v) of the vortex with $y_v = 0.4w$ and $I_{2,0} = 0.2$. Variation of the vortex position leads to substantial modifications in η at low magnetic fields. **d** Sketch of the nanobridge, with SS'S indicating the regions with different amplitudes of the superconducting gap. Here we assume the presence of Rashba and Dresselhaus spin-orbit couplings. Representative skewed and asymmetric CPR (red line) originated by high-harmonic components (up to the third one) and an anomalous phase offset φ_0. **e** Nonreciprocal rectification efficiency η calculated for several values of the third harmonic component $I_{3,0}$, assuming that $I_{1,0} = 1$, $I_{2,0} = -0.3$ and $\Gamma_B = 0.2B/B^*$. η changes sign after maximum rectification is reached. **f** Impact of the fourth harmonic in the rectification, with $I_{1,0} = 1$, $I_{2,0} = -0.3$ and $I_{3,0} = 0.25$.

highly distorted to sinusoidal-like shapes at large temperatures[42,55]. Moreover, as shown in Figs. 2e and 3e, B_{max} is temperature resilient until $T \geq 0.5\ T_c$. This feature is fairly captured by both models, as the maximum rectification looks almost independent of the harmonic content (see Fig. 4b for model I and Fig. 4e for model II). However, long bridges exhibit features that are mostly accounted by model I, while short ones are more compatible with model II. For example, in long (short) bridges the sign reversal is present below (above) B_{max} as shown in Fig. 3b and Fig. 2b to be compared with Fig. 4b and e, respectively. Multiple sign reversal nodes appear in high fields only for long bridges, as shown in Fig. 3b and well described by the interferometric mechanism of model I. While the rectification lineshape given by model II presents only one inversion node. Moreover, the quick damping of the rectification inversion observed at low fields (< 0.3 T) in Fig. 3f is captured by the vortex dynamics described in Fig. 4c. The relative size of the vortex ξ/w is temperature-dependent and influences the vortex position in the bridge. Thus, it is plausible to expect that variations of the vortex size mostly affect the rectification lineshape at low fields while remaining substantially unchanged for larger fields, as shown in Fig. 4c.

Finally, it is interesting to note that by extending the proposed models to in-plane magnetic fields, a sizable supercurrent rectification is anticipated but without sign reversal. In particular, for model I, no phase shift is expected from the spatial dependence of the vector potential, since the orbital coupling between an in-plane field and the electron momentum becomes negligible. Thus, the source of phase interference with the vortex winding is eliminated. For model II, the anomalous phase and the harmonic content would be differently affected by an in-plane Zeeman field compared to the out-of-plane orientation not resulting in sign reversal.

Conclusions

In summary, we have demonstrated the implementation of supercurrent diodes in Nb Dayem nanobridges. By breaking the time-reversal symmetry with an out-of-plane magnetic field, we demonstrate that both the amplitude and sign of the rectification can be tuned without inverting the polarity of the applied field. The evolution of the critical current on B field decays monotonically without showing any skewness, which rules out self-field effects or Meissner currents. We have developed two theoretical models to account for the sources of time- and inversion-symmetry breaking, one based on a vortex phase winding, and one that takes into account the spin-orbit interactions present in polycrystalline heavy materials. Yet, a quantitative description of the supercurrent diode effect in metallic nanoconstrictions should account for both scenarios, which complement each other and can coexist. Furthermore, the fabrication process is simple when compared to that of other platforms, a compelling step towards scalability. Analogous nanobridges can be realized from several elemental superconductors

currently at the base of other architectures, such as nanocryotrons[56], rapid single-flux quanta (RSFQ)[57] and memories[58], which would ease a potential integration.

Finally, the sharp sign reversal of the diode rectification allows us to envisage applications of Dayem nanobridges as B-field threshold detectors. When biased in the vicinity of the rectification node, small variations of an environmental magnetic field would result in modifications of the sign of the rectification parameter.

Methods

Sample fabrication. Nb strips and constrictions are patterned by e-beam lithography on AR-P 679.04 (PMMA) resist. PMMA residuals are removed by O_2-plasma etching after developing. Nb thin films were deposited by sputtering with a base pressure of 2×10^{-8} Torr in a 4 mTorr Ar (6N purity) atmosphere and liftoff by acetone or AR-P 600.71 remover. A thin Ti layer was previously sputtered to improve Nb adhesion and base pressure in the deposition chamber, resulting in a nominal thickness Ti(4nm)/Nb(25nm) and Ti(4nm)/Nb(55nm) for the so-called short and long nanobridges, respectively.

Transport measurements. Transport measurements were carried out in filtered (two-stage RC and π filters) cryogen-free ^{3}He-^{4}He dilution refrigerators by a standard 4-point probe technique. DC current-voltage characteristics were measured by sweeping a low-noise current bias positively and negatively, and by measuring the voltage drop across the weak links with a room-temperature, low-noise preamplifier for each current value every ~20 ms. Current step size ΔI was adapted depending on the switching current keeping the values lower than $0.002 I_{sw}(B=0)$ ~1μ A and 100 nA for short and long devices, respectively. The switching currents are extracted from the maximum of the derivative dV/dI and averaged from 5-10 reiterations of the IV curves. Error bars account for the standard deviation and propagation of errors in I_{sw}, ΔI_{sw}, and η. For the characteristic fields, the error is given by the magnetic field step $\Delta B_z < 10$ mT. Joule heating is minimized by automatically switching the current off once the device turns into the normal state. A delay between sweeps was optimized to keep the stability of the fridge temperature lower than 50 mK. Furthermore, no changes in the switching currents (up to the accuracy given by the standard deviation) were observed in different cooling cycles, by changing the order of the sweeps or by adding an extra delay in the acquisition protocol concluding that hysteretic behavior or local heating is negligible.

Theoretical models. The current phase relation for the model I is given by $I = \sum_{n=1,2} \int_0^w I_n \sin\left(\phi(x) + n\varphi\right) dx$. The critical current in both directions is evaluated by determining the maximum and minimum values with respect to the phase bias φ. Here, the spatial-dependent phase difference $\phi(x)$ is given by the magnetic field and the phase winding contribution due to the vortex[47]. We have assumed that the supercurrent has a subdominant second harmonic contribution, as expected in long, diffusive weak links[42,55]. The spatial dependence of the phase along the transverse direction x is expressed as $\phi(x) = \frac{2\pi d_b B_z x}{\Phi_0} + \phi_v(x)$ where d_b is a characteristic length of the weak link, related to the width of the junction, and $\phi_v(x) = \gamma_v \arctan[\frac{(x-x_v)}{y_v}]$ is the spatially-inhomogeneous phase offset due to the vortex structure. γ_v indicates the sign and amplitude of the winding and (x_v, y_v) the position of the vortex core with respect to the boundaries (see Fig. 4a). We also assume that the second harmonic amplitude of the supercurrent is vanishing at $B = B^*$.

Concerning model II, the current phase relation is given by $I = \sum_n I_n \sin(\varphi) + \Gamma_B \cos(\varphi)$. The critical currents are evaluated by determining the maximum and minimum values of the Josephson current. For the examined model, we assume that the amplitudes of the n-harmonic I_n get suppressed by B with a linear rate, i.e. $I_n = I_{n,0}(1 - \frac{B}{B^*})$ for $n \geq 1$. The linear trend is compatible with the observed behavior of the overall supercurrent amplitude as shown in Figs. 2a and 3a for the range of applied field where the rectification is nonvanishing. Furthermore, the suppression of the amplitude of the harmonics with the magnetic field can be related to the reduction of the effective transmission across the grains due to depairing and magnetic interference. The decrease in the transmission implies a reduction of the non-harmonic amplitudes[42,55]. In this model, we have performed a real space simulation for the examined geometry. By solving the Bogoliubov-de Gennes equations on a finite-size slab in the presence of an out-of-plane magnetic field, we demonstrate that an anomalous phase shift can be obtained. The simulation is performed for a system size $N_x \times N_y$ with $N_x = 150$ and $N_y = 100$. The employed tight-binding model includes a nearest neighbour hopping amplitude t, and the conventional spin-singlet local pairing amplitude. We apply a phase bias across the weak link and determine the free energy as shown in the Supplementary Figure 2a. The resulting anomalous phase increases with the magnetic field and depends on the strength of the Rashba and Dresselhaus interactions as shown in the Supplementary Figure 2b. The linear Rashba term on a lattice for a two-dimensional geometry is expressed as $H_R = \alpha_R[\sin(k_x)\sigma_y - \sin(k_y)\sigma_x]$ while the Dresselhaus term is given by $H_D = \alpha_D[\sin(k_x)\sigma_x - \sin(k_y)\sigma_y]$ with $\sigma_i (i = x, y)$ being the Pauli matrices associated with the spin angular momentum. We notice that H_R breaks the horizontal mirror symmetry while H_D breaks both the vertical and horizontal mirror symmetries. This reduction of mirror symmetry is expected to be locally or globally broken in granular films[54]. Notably, the presence of the Dresselhaus term is crucial to induce an anomalous phase shift in the supercurrent in the presence of an out-of-plane magnetic field.

Concerning the size of the Rashba and Dresselhaus couplings, our analysis shows a sizable, nonvanishing anomalous phase in the presence of an out-of-plane magnetic field for values from 0.01 to 0.3, in units of the effective electron hopping amplitude t. We notice that t is an effective electronic amplitude that describes the low energy properties of the superconductor which can be taken in the order of 20 meV. For such value, Rashba/Dresselhaus couplings able to generate the anomalous phase will range from 0.2 to 6 meV. Although there is no experimental estimations of Rashba and Dresselhaus coupling for Nb thin films, these values are plausible for heavy metals like Nb, since Rashba spin splitting scales with the size of the atomic spin-orbit coupling[59,60]. Nb has a multiorbital electronic structure[61], in this case, the breaking of the inversion or mirror symmetry primarily leads to an orbital Rashba coupling[62,63] among orbitals with different mirror parity. Then, the spin Rashba interaction arises through the atomic spin-orbit coupling. The large amplitude of the atomic spin-orbit coupling in Nb can thus yield a sizable spin Rashba interaction [59,60,64,65].

Data availability

The data that support the findings of this study are available from the corresponding author upon reasonable request.

Code availability

The code that support the findings of this study are available from the corresponding author upon reasonable request.

Received: 10 July 2023; Accepted: 8 November 2023;
Published online: 27 November 2023

References

1. Wakatsuki, R. et al. Nonreciprocal charge transport in noncentrosymmetric superconductors. *Sci. Adv.* **3**, e1602390 (2017).
2. Díez-Mérida, J. et al. Symmetry-broken Josephson junctions and superconducting diodes in magic-angle twisted bilayer graphene. *Nat. Commun.* **14**, 2396 (2023).
3. Lin, J.-X. et al. Zero-field superconducting diode effect in small-twist-angle trilayer graphene. *Nat. Phys.* **18**, 1221–1227 (2022).
4. Paolucci, F., De Simoni, G. & Giazotto, F. A gate-and flux-controlled supercurrent diode effect. *Appl. Phys. Lett.* **122**, 042601 (2023).
5. Ando, F. et al. Observation of superconducting diode effect. *Nature* **584**, 373–376 (2020).
6. Pal, B. et al. Josephson diode effect from cooper pair momentum in a topological semimetal. *Nat. Phys.* **18**, 1228–1233 (2022).
7. Bauriedl, L. et al. Supercurrent diode effect and magnetochiral anisotropy in few-layer NbSe2. *Nat. Commun.* **13**, 4266 (2022).
8. Baumgartner, C. et al. Supercurrent rectification and magnetochiral effects in symmetric Josephson junctions. *Nat. Nanotechnol.* **17**, 39–44 (2022).
9. Jeon, K.-R. et al. Zero-field polarity-reversible Josephson supercurrent diodes enabled by a proximity-magnetized Pt barrier. *Nat. Mater.* **21**, 1008–1013 (2022).
10. Sundaresh, A., Väyrynen, J. I., Lyanda-Geller, Y. & Rokhinson, L. P. Diamagnetic mechanism of critical current non-reciprocity in multilayered superconductors. *Nat. Commun.* **14**, 1628 (2023).
11. Lotfizadeh, N. et al. Superconducting diode effect sign change in epitaxial Al-InAs Josepshon junctions. *arXiv*:2303.01902 (2023).
12. Turini, B. et al. Josephson diode effect in high-mobility InSb nanoflags. *Nano Lett.* **22**, 8502–8508 (2022).
13. Daido, A., Ikeda, Y. & Yanase, Y. Intrinsic superconducting diode effect. *Phys. Rev. Lett.* **128**, 037001 (2022).
14. Ilić, S. & Bergeret, F. S. Theory of the supercurrent diode effect in Rashba superconductors with arbitrary disorder. *Phys. Rev. Lett.* **128**, 177001 (2022).
15. Yuan, N. F. Q. & Fu, L. Supercurrent diode effect and finite-momentum superconductors. *Proc. Natl Acad. Sci.* **119**, e2119548119 (2022).
16. He, J. J., Tanaka, Y. & Nagaosa, N. A phenomenological theory of superconductor diodes. *New J. Phys.* **24**, 053014 (2022).
17. Misaki, K. & Nagaosa, N. Theory of the nonreciprocal Josephson effect. *Phys. Rev. B* **103**, 245302 (2021).
18. Davydova, M., Prembabu, S. & Fu, L. Universal Josephson diode effect. *Sci. Adv.* **8**, eabo0309 (2022).
19. Zhang, Y., Gu, Y., Li, P., Hu, J. & Jiang, K. General theory of Josephson diodes. *Phys. Rev. X* **12**, 041013 (2022).
20. Scammell, H. D., Li, J. I. A. & Scheurer, M. S. Theory of zero-field superconducting diode effect in twisted trilayer graphene. *2D Materials* **9**, 025027 (2022).
21. Wambaugh, J. F., Reichhardt, C., Olson, C. J., Marchesoni, F. & Nori, F. Superconducting fluxon pumps and lenses. *Phys. Rev. Lett.* **83**, 5106–5109 (1999).
22. Vodolazov, D. Y. & Peeters, F. M. Superconducting rectifier based on the asymmetric surface barrier effect. *Phys. Rev. B* **72**, 172508 (2005).
23. Villegas, J. E., Gonzalez, E. M., Gonzalez, M. P., Anguita, J. V. & Vicent, J. L. Experimental ratchet effect in superconducting films with periodic arrays of asymmetric potentials. *Phys. Rev. B* **71**, 024519 (2005).
24. Van de Vondel, J., de Souza Silva, C. C., Zhu, B. Y., Morelle, M. & Moshchalkov, V. V. Vortex-rectification effects in films with periodic asymmetric pinning. *Phys. Rev. Lett.* **94**, 057003 (2005).
25. Carapella, G., Granata, V., Russo, F. & Costabile, G. Bistable Abrikosov vortex diode made of a Py-Nb ferromagnet-superconductor bilayer structure. *Appl. Phys. Lett.* **94**, 242504 (2009).
26. Cerbu, D. et al. Vortex ratchet induced by controlled edge roughness. *New J. Phys.* **15**, 063022 (2013).
27. Golod, T. et al. Reconfigurable Josephson Phase Shifter. *Nano Lett.* **21**, 5240–5246 (2021).
28. Lyu, Y.-Y. et al. Superconducting diode effect via conformal-mapped nanoholes. *Nat. Commun.* **12**, 2703 (2021).
29. Golod, T. & Krasnov, V. M. Demonstration of a superconducting diode-with-memory, operational at zero magnetic field with switchable nonreciprocity. *Nat. Commun.* **13**, 3658 (2022).
30. Suri, D. et al. Non-reciprocity of vortex-limited critical current in conventional superconducting micro-bridges. *Appl. Phys. Lett.* **121**, 102601 (2022).
31. Chahid, S., Teknowijoyo, S., Mowgood, I. & Gulian, A. High-frequency diode effect in superconducting Nb_3Sn microbridges. *Phys. Rev. B* **107**, 054506 (2023).
32. Hou, Y. et al. Ubiquitous superconducting diode effect in superconductor thin films. *Phys. Rev. Lett.* **131**, 027001 (2023).
33. Satchell, N., Shepley, P. M., Rosamond, M. C. & Burnell, G. Supercurrent diode effect in thin film Nb tracks. *J. Appl. Phys.* **133**, 203901 (2023).
34. Vávra, O., Pfaff, W., Monaco, R., Aprili, M. & Strunk, C. Current-controllable planar S-(S/F)-S Josephson junction. *Appl. Phys. Lett.* **102**, 072602 (2013).
35. Costa, A. et al. Sign reversal of the Josephson inductance magnetochiral anisotropy and 0-π-like transitions in superconducting diodes. *Nat. Nanotechnol.*1–7 (2023).
36. Kawarazaki, R. et al. Magnetic-field-induced polarity oscillation of superconducting diode effect. *Appl. Phys. Express.* **15**, 113001 (2022).
37. Gupta, M. et al. Gate-tunable superconducting diode effect in a three-terminal Josephson device. *Nat. Commun.* **14**, 3078 (2023).
38. Gillijns, W., Silhanek, A. V., Moshchalkov, V. V., Reichhardt, C. J. O. & Reichhardt, C. Origin of reversed vortex ratchet motion. *Phys. Rev. Lett.* **99**, 247002 (2007).
39. He, A., Xue, C. & Zhou, Y.-H. Switchable reversal of vortex ratchet with dynamic pinning landscape. *Appl. Phys. Lett.* **115** (2019).
40. Ideue, T., Koshikawa, S., Namiki, H., Sasagawa, T. & Iwasa, Y. Giant nonreciprocal magnetotransport in bulk trigonal superconductor $PbTaSe_2$. *Phys. Rev. Res.* **2**, 042046 (2020).
41. Jiang, J. et al. Reversible ratchet effects in a narrow superconducting ring. *Phys. Rev. B* **103**, 014502 (2021).
42. Likharev, K. K. Superconducting weak links. *Rev. Mod. Phys.* **51**, 101–159 (1979).
43. Jani, A. R., Brener, N. E. & Callaway, J. Band structure and related properties of bcc niobium. *Phys. Rev. B* **38**, 9425–9433 (1988).
44. Skocpol, W. J., Beasley, M. R. & Tinkham, M. Self-heating hotspots in superconducting thin-film microbridges. *J. Appl. Phys.* **45**, 4054–4066 (2003).
45. Aranson, I., Gitterman, M. & Shapiro, B. Y. Motion of vortices in thin superconducting strips. *J. Low Temp. Phys.* **97**, 215–228 (1994).
46. Aranson, I., Gitterman, M., Shapiro, B. Y. & Vinokur, V. Nucleation, growth and kinetics of the vortex phase in thin superconducting strips. *Phys. Scrip.* **1996**, 125 (1996).
47. Krasnov, V. M. Josephson junctions in a local inhomogeneous magnetic field. *Phys. Rev. B* **101**, 144507 (2020).
48. Assouline, A. et al. Spin-orbit induced phase-shift in Bi2Se3 Josephson junctions. *Nat. Commun.* **10**, 126 (2019).
49. Strambini, E. et al. A Josephson phase battery. *Nat. Nanotechnol.* **15**, 656–660 (2020).
50. Mayer, W. et al. Gate controlled anomalous phase shift in Al/InAs Josephson junctions. *Nat. Commun.* **11**, 212 (2020).
51. Margineda, D., Claydon, J. S., Qejvanaj, F. & Checkley, C. Observation of anomalous Josephson effect in nonequilibrium Andreev interferometers. *Phys. Rev. B* **107**, L100502 (2023).
52. Machin, D. J. & Sullivan, J. F. The preparation and properties of complexes derived from niobium(IV) halides. *J. less-common met.* **19**, 405–411 (1969).
53. Gül, Ö. et al. Andreev Reflection in the Fractional Quantum Hall State. *Phys. Rev. X* **12**, 021057 (2022).
54. Park, J.-S. Stabilization and self-passivation of symmetrical grain boundaries by mirror symmetry breaking. *Phys. Rev. Mater.* **3**, 014602 (2019).
55. Golubov, A. A., Kupriyanov, M. Y. & Il'ichev, E. The current-phase relation in Josephson junctions. *Rev. Mod. Phys.* **76**, 411–469 (2004).
56. McCaughan, A. N. & Berggren, K. K. A superconducting-nanowire three-terminal electrothermal device. *Nano Lett.* **14**, 5748–5753 (2014).
57. Likharev, K. K. & Semenov, V. K. Rsfq logic/memory family: A new Josephson-junction technology for sub-terahertz-clock-frequency digital systems. *IEEE Trans. Appl. Supercond.* **1**, 3–28 (1991).
58. Ligato, N., Strambini, E., Paolucci, F. & Giazotto, F. Preliminary demonstration of a persistent Josephson phase-slip memory cell with topological protection. *Nat. Commun.* **12**, 5200 (2021).
59. Sunko, V. et al. Maximal Rashba-like spin splitting via kinetic-energy-coupled inversion-symmetry breaking. *Nature* **549**, 492–496 (2017).
60. Bihlmayer, G., Noël, P., Vyalikh, D. V., Chulkov, E. V. & Manchon, A. Rashba-like physics in condensed matter. *Nat. Rev. Phys.* **4**, 642–659 (2022).
61. Rüßmann, P. & Blügel, S. Density functional Bogoliubov-de Gennes analysis of superconducting Nb and Nb(110) surfaces. *Phys. Rev. B.* **105**, 125143 (2022).
62. Park, S. R., Kim, C. H., Yu, J., Han, J. H. & Kim, C. Orbital-Angular-Momentum Based Origin of Rashba-Type Surface Band Splitting. *Phys. Rev. Lett.* **107**, 156803 (2011).
63. Mercaldo, M. T., Solinas, P., Giazotto, F. & Cuoco, M. Electrically Tunable Superconductivity Through Surface Orbital Polarization. *Phys. Rev. Appl.* **14**, 034041 (2020).

64. Ishizaka, K. et al. Giant Rashba-type spin splitting in bulk BiTeI. *Nat. Mater.* **10**, 521–526 (2011).
65. Yaji, K. et al. Large Rashba spin splitting of a metallic surface-state band on a semiconductor surface. *Nat. Commun.* **1**, 17 (2010).

Acknowledgements

This work was funded by the EU's Horizon 2020 Research and Innovation Framework Program under Grant Agreement No. 964398 (SUPERGATE), No. 101057977 (SPECTRUM), and by the PNRR MUR project PE0000023-NQSTI.

Author contributions

D.M. fabricated the samples, conducted the experiments, and analyzed data with inputs from A.C., E.S. and F.G. The theoretical models describing the experiment was developed by Y.F., M.T.M., and M.C. The manuscript was written by D.M., A.C., E.S., M.C., and F.G. with inputs from all the authors. E.S. and F.G. conceived the experiment. F.G. supervised and coordinated the project. All authors discussed the results and their implications equally at all stages.

Competing interests

The authors declare no competing interests.

Additional information

Supplementary information The online version contains supplementary material available at https://doi.org/10.1038/s42005-023-01458-9.

Correspondence and requests for materials should be addressed to Daniel Margineda or Francesco Giazotto.

Peer review information *Communications Physics* thanks the anonymous reviewers for their contribution to the peer review of this work. A peer review file is available.

Reprints and permission information is available at http://www.nature.com/reprints

Publisher's note Springer Nature remains neutral with regard to jurisdictional claims in published maps and institutional affiliations.

Open Access This article is licensed under a Creative Commons Attribution 4.0 International License, which permits use, sharing, adaptation, distribution and reproduction in any medium or format, as long as you give appropriate credit to the original author(s) and the source, provide a link to the Creative Commons licence, and indicate if changes were made. The images or other third party material in this article are included in the article's Creative Commons licence, unless indicated otherwise in a credit line to the material. If material is not included in the article's Creative Commons licence and your intended use is not permitted by statutory regulation or exceeds the permitted use, you will need to obtain permission directly from the copyright holder. To view a copy of this licence, visit http://creativecommons.org/licenses/by/4.0/.

© The Author(s) 2023